A Real-Time Optical Sensor for Simultaneous Measurement of Three-DOF Motions

Kok-Meng Lee and Debao Zhou

***Abstract*—The need for simultaneous measurement of multiple degree-of-freedom (DOF) motions can be found in numerous applications such as robotic assembly, precision machining, optical tracking, wrist actuators, and active joysticks. Conventional single-axis encoders, though capable of providing high-resolution (linear or angular) measurements, rely on mechanical linkages (that often introduce frictions, backlashes, and singularities) to constrain the device so that the three-DOF (3-DOF) motion can be deduced from the individual orthogonal measurements. We present here a noncontact optical sensor for 3-DOF planar and spherical orientation measurements. We begin with the operational principle of a microscopic-surface-based optical sensor. The design concept and theory of a dual-sensor system capable of measuring 3-DOF planar and spherical motions in real time are then presented. Along with a detailed analysis, the concept feasibility of two prototype 3-DOF dual-sensor systems for measuring the instantaneous center of rotation and the angular displacement of a moving surface is demonstrated experimentally. It is expected that the analysis will serve as a basis for optimizing key design parameters that could significantly influence the sensor performance.**

***Index Terms*—Encoder, optical sensor, orientation measurement, spherical sensor.**

I. Introduction

VISION-BASED sensing (also called optical gauging) is a technique for making displacement measurements based on the relative position of some types of patterns or features in the field of a vision sensor. These sensing methods have been used in many areas such as the alignment of contact lenses using fiducial marks, automobile wheel alignment, and alignment, docking, and assembly tasks related to the construction of the International Space Station [5], [10]. In this paper, we offer an alternative design of an optical sensor for simultaneous measurement of three-degree-of-freedom (3-DOF) planar and spherical motions.

The use of single-axis encoders for measuring 3-DOF motions often requires a mechanism to constrain the device so that the 3-DOF motion can be deduced from the three individual orthogonal measurements. The desire to eliminate the constraining mechanism, which often introduces significant friction and inertia, has motivated Lee [8] to develop alternative image-based methods for measuring the 3-DOF orientation of a spherical body. Unlike conventional video-based systems that require pixel data of a full image frame to be stored in a video buffer before processing of data can commence, the 3-DOF orientation sensor use a flexible-integrated-vision system [9] to provide an option to completely bypass the video buffer and thus offers a means to process and/or to store the digitized pixel data by a microprocessor. Most recently, rapid increase in demands for high-performance pointing devices (such as a computer input mouse) for use with a personal computer has provided the incentives for the development of high-resolution optical sensors for measuring 2-DOF translational motions [3]. The sensor for the pointing device generates pulses proportional to the relative motion of the sensor with respect to a static surface. The number of pulses is derived from the detection of microscopic changes of surface features between consecutive images; no engineered patterns (such as interferometer grating) are needed. These attractive features have provided the incentives for further development of an optical encoder, which can measure the instantaneous center of rotation and the angular displacement of a moving surface.

While the optical sensor for a pointing device is capable of detecting changes on the order of 1500 frames per second (fps), the sensor is indifferent to the rotation about its own optical axis. Moreover, since these optical sensors are primarily developed for use as a user-operated pointing device, there has been no design theory to help develop the sensor for use as a machine-operated motion sensor. For these reasons, we offer here the following:

1) the operational principle of a microscopic-surface-based optical sensor;
2) two prototype dual-sensor systems capable of measuring a 3-DOF planar motion in real time;
3) a detailed analysis with experimental verification, which serves an essential basis for optimizing the sensor design.

II. Operational Principle of a Microscopic-Feature-Based 3-DOF Planar Encoder

Fig. 1 shows the components making up a basic imaging system that consists of a photodetector, a light source such as a light-emitting diode (LED) that illuminates the surface, and a lens that collects the reflected light and forms an image on the photodetector. For detecting microscopic features, the sensor/LED unit is placed very close to the surface, and thus, the illuminated area is essentially circular. The displacement of the moving surface beneath the optical sensor (faced down) can be determined by analyzing the changes in two consecutive images (I_{i-1} and I_i) as illustrated in Fig. 2, where the black pixels represent the common area in both images, while hashed pixels are the intensity changes as detected by the sensor.

Manuscript received January 15, 2004; revised April 15, 2004 and June 16, 2004.

The authors are with the G. W. Woodruff School of Mechanical Engineering, Georgia Institute of Technology, Atlanta, GA 30332-0405, USA (e-mail: kokmeng.lee@me.gatech.edu; gte090x@prism.gatech.edu).

Digital Object Identifier 10.1109/TMECH.2004.834642

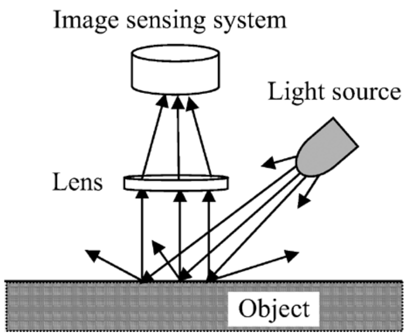

Fig. 1. Typical imaging system.

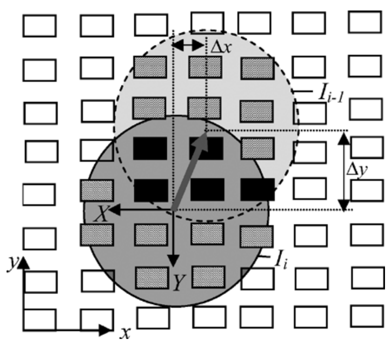

Fig. 2. Surfaces captured by two consecutive images.

In Fig. 2, the reference frame *XYZ* is located at the optical center of the imaging sensor, while xyz is fixed on the moving surface. The directions of (X, Y) and (x, y) are assigned such that the displacement of the moving surface and that viewed by the fixed sensor have the same sign algebraically. The instantaneous velocity of the moving surface at a particular time instant can be expressed as

$$\mathbf{v} = v_x\hat{x} + v_y\hat{y} \tag{1}$$

and

$$\begin{bmatrix} v_x \\ v_y \end{bmatrix} = \frac{1}{t_c}\begin{bmatrix} \Delta x \\ \Delta y \end{bmatrix} = \frac{1}{C_i t_c}\begin{bmatrix} C_x \\ C_y \end{bmatrix} \tag{2}$$

where $\hat{x}$ and $\hat{y}$ are unit vectors of the X and Y axes, t_c is the cycle time, C_i is the counts per inch (cpi) for the sensor, and $(\Delta X, \Delta Y)$ and (C_x, C_y) are the incremental distance traveled and the corresponding sensor output (in number of counts) within a cycle. The optical sensor, however, is indifferent to the rotation about its own optical axis. Thus, more than one sensor is needed in order to measure the rotation of a plane.

To derive the sensor kinematics that allow for the application of two or more sensors for measuring 3-DOF motions, we define the coordinate systems in Fig. 3 where the subscript k denotes the kth sensor. In Fig. 3, we attach an xyz coordinate system on the moving surface that translates relative to the reference frame XYZ at a velocity $\mathbf{v}_0$ and rotates at an angular velocity ω about $\hat{z}$ (the unit vector of the z axis), where the directions of the z and Z axes follow the right-hand rule. Similarly, we define the coordinate system $X_kY_kZ_k$ of the kth optical sensor at O_k, a point fixed in XYZ frame; for example, the origin of the kth sensor is assigned at $X = -d_k$, $Y = -h_k$. In addition, we further define in Fig. 3 the following to facilitate the discussion:

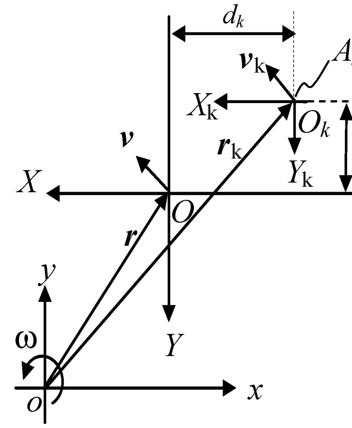

Fig. 3. Sensor coordinates.

- A_k a point located directly beneath O_k (or the origin of the sensor coordinate system $X_kY_kZ_k$) but on the moving surface;
- $\mathbf{r}$ a position vector from the origin of xyz frame to the origin of the reference frame XYZ;
- $\mathbf{r}_k$ a position vector from the origin of xyz frame to the point A_k.

Thus, the velocity of the point A_k, $\mathbf{v}_k$ is given by

$$\mathbf{v}_k = \mathbf{v}_0 + \mathbf{r}_k \times \boldsymbol{\omega} \tag{3}$$

where

$$\boldsymbol{\omega} = \omega\hat{z} \tag{4}$$

and $\mathbf{v}_0$ is the velocity at the origin o (or the origin of the moving surface frame xyz). The motion of the plane can be broadly classified into the following cases.

Case 1: 1-DOF rotation ($\boldsymbol{v_o} = \mathbf{0}$ and $\mathbf{r} = \mathbf{0}$)

The surface beneath the kth sensor rotates about the Z axis. The instantaneous angular velocity is given by

$$\omega = \frac{1}{r_k}|\boldsymbol{v_k}|\hat{\boldsymbol{Z}} \tag{5}$$

provided $r_k \neq 0$, ω can be determined using one sensor.

Case 2: 2-DOF translation ($\omega = 0$)

The instantaneous velocity of the translating surface, as read by the fixed sensor, is given by (2). The displacements in X and Y directions can be found by integrating the respective velocity components over time.

Case 3: 3-DOF planar motion $\boldsymbol{v_o} = \mathbf{0}$ and $\mathbf{r} \neq 0$

The three unknowns in the planar motion measurement are the instantaneous center of the rotation, and the angular velocity about the z-axis. Consider two identical sensors ($k = 1$ and 2) as shown in Fig. 4, the velocity of a point directly below O_k on the moving surface is given by

$$\mathbf{v}_k = \boldsymbol{\omega} \times \mathbf{r}_k \tag{6}$$

or

$$\mathbf{v}_k = \begin{bmatrix} -\omega(y + h_k) \\ \omega(x + d_k) \end{bmatrix} \tag{7}$$

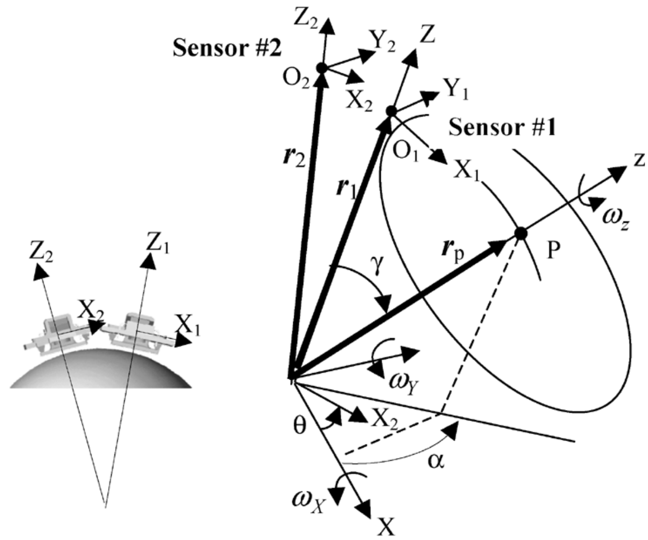

Fig. 4. Coordinate systems.

where

$$\mathbf{r}_k = (x + d_k)\hat{\boldsymbol{x}} + (y + h_k)\hat{\boldsymbol{y}} \tag{8}$$

The instantaneous velocity of the surface (as viewed by the fixed dual-sensor system) is given by (2) and thus (7) can be written as

$$\frac{1}{t_c}\begin{bmatrix}\Delta x_k \\ \Delta y_k\end{bmatrix} = \begin{bmatrix}-\omega(y + h_k) \\ \omega(x + d_k)\end{bmatrix}. \tag{9}$$

For the dual-sensor system, it can be shown that only 3 of the four equations given by (9) where $k = 1$, and 2 are independent since both sensors would have the same reading in the direction along the line connecting the optical center.

For simplicity, we let $h_1 = h_2 = 0$ implying that the two identical sensors are mounted on the X-axis and hence

$$\Delta x_1 = \Delta x_2. \tag{10}$$

The angular velocity ω is then given by

$$\omega = \frac{\Delta y_1 - \Delta y_2}{(d_1 - d_2)t_c} \tag{11}$$

and the instantaneous center of rotation, (x, y) is at

$$x = \frac{1}{2}\left[\frac{\Delta y_1 + \Delta y_2}{\omega t_c} - (d_1 + d_2)\right] \tag{12a}$$

and

$$y = \frac{-\Delta x_k}{\omega t_c}. \tag{12b}$$

The angular displacement of the surface can then be calculated from the following integral:

$$\theta = \int_{t=0}^{nt_c} \omega dt \approx \left(\frac{1}{d_1 - d_2}\right)\sum_{i=1}^{n}(\Delta y_1 - \Delta y_2) \tag{12c}$$

where n is the number of cycles. As an example, consider $h_1 = h_2 = 0$ and $d_1 = -d_2 = d/2 = 14.38$ mm (0.575 inch).

$$\omega = \frac{C_{y1} - C_{y2}}{dC_i t_c} \tag{13a}$$

$$x = \frac{1}{2}\left[\frac{C_{y1} + C_{y2}}{\omega t_c C_i}\right] \tag{13b}$$

$$y = \frac{-C_{x1}}{\omega t_c C_i} \tag{13c}$$

For an optical sensor with a linear resolution of 500 cpi, the resolution of the angular displacement with a cycle time t_c is in the order of 0.1° for a given d of 28.76 mm.

III. 3-DOF Spherical Orientation Encoder

The dual-sensor system can be used to measure the 3-DOF rotational motions of a spherical wrist, where the center of rotation is fixed as illustrated in Fig. 4. In Fig. 4, XYZ and xyz are the reference and the body-fixed coordinate frames attached at the centers of the stator and the rotor, respectively. The z-axis intersects with the spherical rotor surface at point P and its unit vector $\hat{\mathbf{z}}$ can be expressed in the XYZ frame as

$$\hat{\mathbf{z}} = [\sin\gamma\cos\alpha \quad \sin\gamma\sin\alpha \quad \cos\gamma]^T \tag{14}$$

where γ is the angle between the Z and the z axes, and α is the angle between the projection of the z-axis on the XY plane and the X axis.

The two sensors are placed such that their optical axes meet at the spherical center but are spaced by an angle θ. Without loss of generality, we consider that one of the two sensors is located along the Z axis on the spherical stator at O_1 as shown in Fig. 4. The second sensor is placed on the same spherical surface at O_2 such that its optical axis is on the XZ plane. Thus, the locations of O_1 and O_2 are given by

$$\boldsymbol{r}_k = [-R\sin\theta_k \quad 0 \quad R\cos\theta_k]^T, \quad (k = 1, 2) \tag{15}$$

where $\theta_1 = 0$, $\theta_2 = \theta$, and R is the radius of the rotor.

As an illustration, we develop a sensor model for measuring the rotor motion of a spherical wrist, which can be mathematically described by the following equation:

$$\boldsymbol{\omega} = \omega_X\hat{\mathbf{X}} + \omega_Y\hat{\mathbf{Y}} + \omega_z\hat{\mathbf{z}} \tag{16}$$

where ω_X, ω_Y, and ω_z are the angular velocities about the $\hat{\mathbf{X}}$, $\hat{\mathbf{Y}}$ (the unit vectors of the X and Y axes), and $\hat{\mathbf{z}}$, respectively.

A. Forward Kinematics

The forward kinematics simulates the instantaneous readouts of the sensors for a specified angular velocity of the rotor, which can be expressed in the stator (XYZ) frame:

$$\boldsymbol{\omega} = (\omega_X + \omega_z\sin\gamma\cos\alpha)\hat{\mathbf{X}} + (\omega_Y + \omega_z\sin\gamma\sin\alpha)\hat{\mathbf{Y}} + \omega_z\cos\gamma\hat{\mathbf{Z}}. \tag{17}$$

Thus, the velocity of point O_k on the rotor surface in the XYZ frame can be computed from $\mathbf{v}_k = \boldsymbol{\omega} \times \mathbf{r}_k$ where $\boldsymbol{\omega}$ and $\boldsymbol{r_k}$ are given by (15) and (17), respectively, or

$$\begin{bmatrix} v_{xk} \\ v_{yk} \end{bmatrix} = R \begin{bmatrix} 0 & 1 & \sin\gamma\sin\alpha \\ -\cos\theta_k & 0 & -\sin\gamma\sin\theta_k - \cos\theta_k\sin\gamma\cos\alpha \end{bmatrix} \begin{bmatrix} \omega_X \\ \omega_Y \\ \omega_z \end{bmatrix}.$$

Consider the two sensors configured in (15), and note that only three of the four equations are independent:

$$\begin{bmatrix} v_{x1} \\ v_{y1} \\ v_{y2} \end{bmatrix} = R \begin{bmatrix} 0 & 1 & \sin\gamma\sin\alpha \\ -1 & 0 & -\sin\gamma\cos\alpha \\ -c_\theta & 0 & -s_\theta\cos\gamma - c_\theta\sin\gamma\cos\alpha \end{bmatrix} \begin{bmatrix} \omega_X \\ \omega_Y \\ \omega_z \end{bmatrix} \tag{18}$$

where $c_\theta = \cos\theta$ and $s_\theta = \sin\theta$.

B. Inverse Kinematics

The inverse kinematics recovers the rotor orientation (the inclination and spin angle of the shaft) from the instantaneous readouts of the sensor. In order to derive the solution in closed form for implementation in real time, we have made the following assumptions.

1) The cycle is short such that $\boldsymbol{\omega} \approx \Delta\boldsymbol{\phi}/\Delta\mathrm{t} = \Delta\boldsymbol{\phi}/\mathrm{t_c}$.
2) The initial values are known such that

$$\begin{aligned}\phi_{i+1} &= \phi_i + \Delta\phi_i \\ &= [\phi_{X,i} + \Delta\phi_{X,i} \quad \phi_{Y,i} + \Delta\phi_{Y,i} \quad \phi_{z,i} + \Delta\phi_{z,i}]^T\end{aligned}$$

and the coordinate of point P, $\mathbf{r}_p$ or (x_p, y_p, z_p) is given by

$$x_P = z_P \tan(\phi_{Y,i} + \Delta\phi_{Y,i}) \tag{19a}$$
$$y_P = z_P \tan(\phi_{X,i} + \Delta\phi_{X,i}) \tag{19b}$$
$$x_P^2 + y_P^2 + z_P^2 = R^2. \tag{19c}$$

3) Changes are small within the cycle such that

$$\sin(\alpha + \Delta\alpha) \approx \sin\alpha + \Delta\alpha\cos\alpha$$
$$\text{and} \quad \cos(\alpha + \Delta\alpha) \approx \cos\alpha + \Delta\alpha\sin\alpha.$$

Based on the above assumptions, the incremental (X, Y, and z) rotations in the ith cycle are derived from (19):

$$\begin{bmatrix} \Delta\phi_{X,i} \\ \Delta\phi_{Y,i} \\ \Delta\phi_{z,i} \end{bmatrix} = \frac{1}{Rs_\theta c_\gamma} \begin{bmatrix} 0 & s_\theta c_{\gamma i} + c_\theta s_{\gamma i} c_{\alpha i} & s_{\gamma i} c_{\alpha i} \\ s_\theta c_{\gamma i} & -c_\theta s_{\gamma i} s_{\alpha i} & s_{\gamma i} s_{\alpha i} \\ 0 & c_\theta & -1 \end{bmatrix} \begin{bmatrix} \Delta x_{1,i} \\ \Delta y_{1,i} \\ \Delta y_{2,i} \end{bmatrix} \tag{20}$$

where

$$\gamma_i \neq \frac{\pi}{2} \quad \text{and} \quad \theta \neq 0$$

and $c_{\gamma i} = \cos\gamma_i$, $c_{\alpha i} = \cos\alpha_i$, $s_{\gamma i} = \sin\gamma_i$, and $s_{\alpha i} = \sin\alpha_i$. Furthermore

$$\mathbf{r}_p = R \begin{pmatrix} \sin(\gamma_i + \Delta\gamma_i)\cos(\alpha_i + \Delta\alpha_i) \\ \sin(\gamma_i + \Delta\gamma_i)\sin(\alpha_i + \Delta\alpha_i) \\ \cos(\gamma_i + \Delta\gamma_i) \end{pmatrix}. \tag{21}$$

The shaft inclination at the $(i+1)$th cycle can be solved from (19) and (21), which yield

$$\alpha_{i+1} \approx \alpha_i + \Delta\alpha_i = \mathrm{a}\tan 2 \left(\frac{\tan(\phi_{X,i} + \Delta\phi_{X,i})}{\tan(\phi_{Y,i} + \Delta\phi_{Y,i})} \right) \tag{22a}$$

$$\gamma_{i+1} \approx \gamma_i + \Delta\gamma_i = \cos^{-1}\left(\frac{1}{\sqrt{1 + \tan^2(\phi_{Y,i} + \Delta\phi_{Y,i}) + \tan^2(\phi_{X,i} + \Delta\phi_{X,i})}} \right). \tag{22b}$$

For completeness, the spin angle is

$$\varphi_{i+1} \approx \varphi_i + \Delta\phi_{z,i} \tag{22c}$$

where $0 \le \gamma_{i+1} < \pi/2$ and $\pi \le \alpha_{i+1} < -\pi$.

C. Computational Singularities

For $\theta \neq 0$, there are two computational singularities in the inverse kinematics.

1) When $|\phi_{Y,i} + \Delta\phi_{Y,i}| = 0$, (22a) becomes singular, which corresponds to $\gamma_i = \alpha_i = 0$ (i.e., z and Z axes are coincident). It can be shown with (18) that

$$\Delta\phi_{X,i} = -\frac{\Delta y_1}{R}$$
$$\Delta\phi_{Y,i} = \frac{\Delta x_1}{R}$$
$$\Delta\phi_X = \frac{\Delta y_2 - \Delta y_1\cos\theta}{R\cos\theta}.$$

2) Equation (20) becomes singular when $\gamma_i = \pi/2$, which corresponds to $|\phi_{Y,i} + \Delta\phi_{Y,i}| = \pi/2$ or $|\phi_{X,i} + \Delta\phi_{X,i}| = \pi/2$ in (22b). For joints with a working range of $\gamma < \pi/2$, this generally does not pose a problem.

IV. Experimental Prototypes

Along with a detailed study on the design sensitivities of a typical microscopic-feature-based sensor on its performance for machine uses, we present two prototypes (a planar and a spherical) to demonstrate the concept feasibility of the dual-sensor system for measuring 3-DOF motions.

A. Optical Sensor Assembly

Fig. 5(a) shows an exploded view of the sensor assembly that consists of an optical sensor [2], an LED, and lenses. The light path of the optical sensor is shown in Fig. 5(b) and the signal processing of the optical sensor is illustrated in Fig. 6. The optical sensor outputs two pairs of quadrature signals: (XA, XB) and (YA, YB) to a decoding circuit designed at Georgia Tech to facilitate the communication between the optical sensor and an external microcomputer. The decoding circuit consists of a pair of HP HCTL-2000 chips [1] and a Keithley KPCI-3130 DIO card [7]. The 12-bit output data of each decoder is organized in two bytes (8 lower and 4 higher bits), which are read by the eight digital lines of the Keithley DIO card via the digital control signals SEL, OE, and $\overline{\mathrm{RST}}$.

The dual-sensor system uses four decoders to convert four pairs of quadrature signals to two sets of x and y displacements.

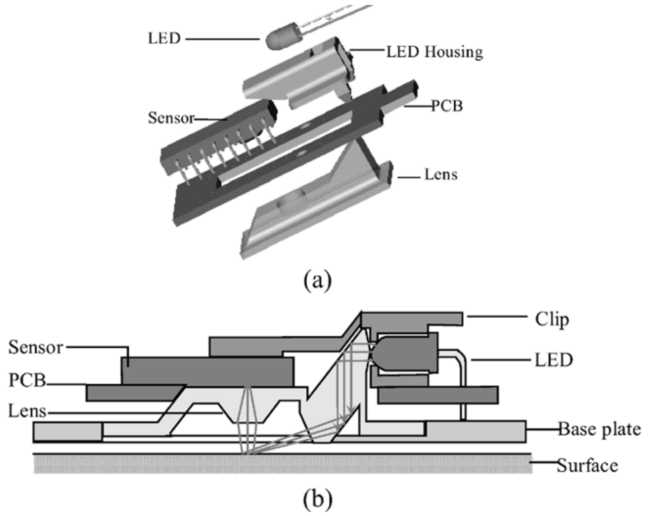

Fig. 5. Optical sensor schematic. (a) Exploded view of an optical sensor; (b) assembly view illustrating the principle.

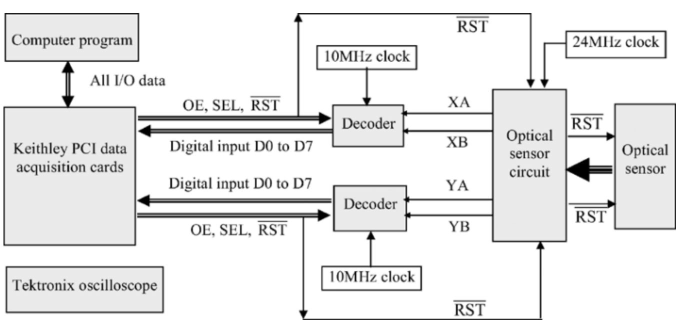

Fig. 6. Signal processing of the sensor.

Each of the decoders requires eight digital data lines and eight digital control signal lines ($\overline{\mathrm{RST}}$, SEL, and OE). Two Keithley KP-3130 cards are needed to accommodate the 44 digital lines; one of these provides (4 × 8) 32 digital I/O data and the other is used to send signals for data-reading control.

Software was written using MS C++ to execute the following tasks. 1) Send digital control signals to read and clear data. 2) Read the 2-byte data from the decoders. 3) Convert the 2-byte data to x and y counts, C_{xk} and C_{yk}. 4) Calculate the motion variables, x, y, and ω. 5) Save and display data for debugging.

B. Effects of Surface Property on Resolution

The effects of the surface property on the resolution of the optical sensor were studied on Test setup #1 as shown in Fig. 7(a), which consists of a precision NSF ball-screw (120-mm long) and a dual-optical-sensor system mounted on a beam. As shown in Fig. 7(a), the two sensors are housed in a holder with an external dimension equal to 70 mm × 70 mm × 12.5 mm. The translational motion of the sensor was measured by means of an LVDT and a micrometer-depth-gauge that has a resolution of 0.025 mm (or 0.001 inch). Table I compares the resolutions in cpi for several different surfaces. Since the sensor detects microscopic changes as it moves over the surface, surfaces that are characterized by its high irregularities (such as a photocopy of sandpaper) are more desired than uniform surfaces (such as

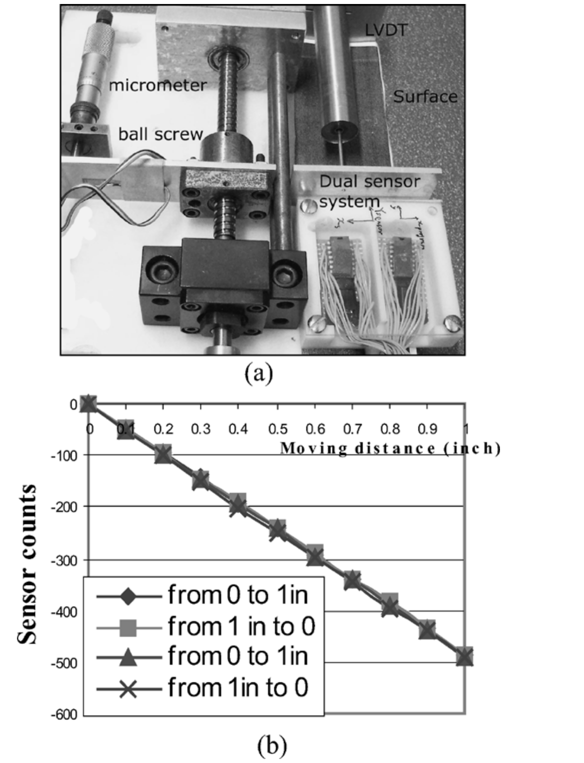

Fig. 7. Sensor repeatability ($C_i = 495$ cpi). (a) Test setup #1. (b) Test results.

TABLE I
EFFECT OF SURFACE PROPERTIES ON C_i

Surface property	Counts per inch
White copier paper	0
Glossy metallic painted finish	23
Black characters on white paper	120
Smooth table surface	335
Dot pattern cloth	495
Photocopy of a sand paper	495

white paper) as expected. Fig. 7(b) plots the reading of the optical sensor manually moved over a photocopy of sandpaper (Aluminum Oxide 220 grit manufactured by Ali-Gator-Grit), for which the resolutions in both X and Y directions were determined to be 495 cpi.

C. Effects of Sensor-Surface Spacing

The effects of the spacing between the sensor and the rotating surface on sensor errors were experimentally studied using the setup shown in Fig. 8(a), where the dc servomotor rotates a plane surface (120-mm diameter) about its shaft. The speed servo took the reference input signal from a Tecktronix TM504 Signal Generator. Controlled by a Copley Motion Controller [4], the speed of the servomotor was measured by the tachometer and digitized using a Keithley ADS1602 [6] so that comparisons between the tachometer readings and those measured by the dual-sensor system can be made. The flowchart of the computer program is shown in Fig. 8(b). The motion parameters are then computed using a 650 MHz Pentium III PC. The sensor-surface spacing is monitored by a micrometer dial gauge that has a resolution of 0.001 in, as shown in Fig. 9(a). The dual-sensor measured the displacement of the rotating surface for a specified number

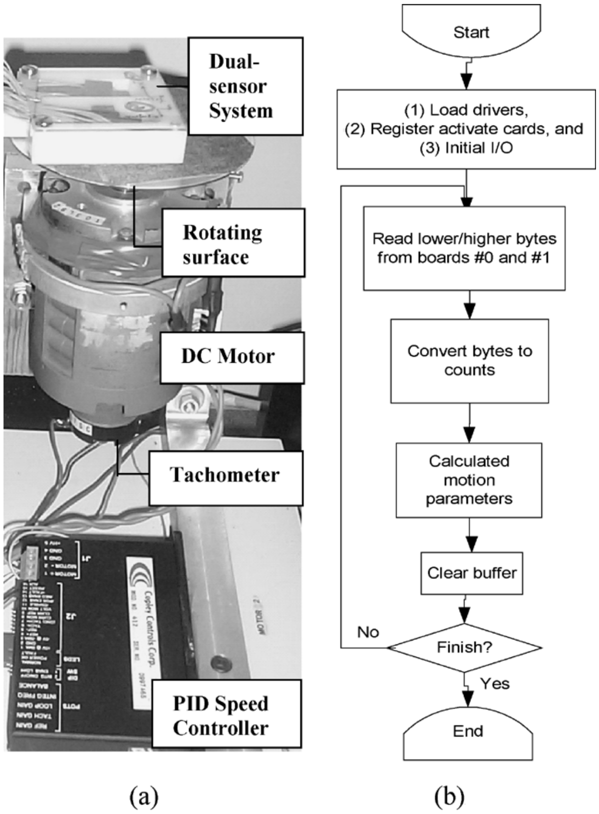

Fig. 8. Planar dual-sensor system. (a) Test setup #2. (b) Algorithm flowchart.

of rotations for a given spacing. It has been observed that the minimum loss count occurs when the sensor-surface spacing is about 2.4 mm. Other results are summarized in Fig. 9.

The same setup was used to examine the repeatability of the sensor, we registered the x and y counts of the sensor as the surface is rotated arbitrarily back and forth. Fig. 10(a) show the typical x-counts as a function of time. The locus of a point passing beneath the optical center is essentially part of a circle with respect to the rotating axis. However, the points passing below the optical center appear as a straight line relating the x and y counts as perceived by the optical sensor. The slope of this straight line in Fig. 10(b) is proportional to the inclination of the line connecting the optical center O and the axis of rotation. As shown in Fig. 10(a), a point corresponding to $x = 2000$ counts passes the optical center 6 times and consistently yields $y = -3000$ counts as shown in Fig. 10(b), which demonstrates that the optical sensor exhibits an excellent repeatability.

D. Measuring Three-DOF Planar Motions

To validate the inverse kinematics of the planar sensor, (13a)–(13c), experiments were conducted to compare the sensor readings against those measured by the tachometer using the setup shown Fig. 8. In these measurements, the relative position of the sensor with respect to the motor shaft remains fixed. Figs. 11 and 12 compare the measurements for two different types of input to the dc motor, namely, a sinusoidal wave and a square wave. As shown in Figs. 11(a) and 12(a), the angular speeds computed by the dual-sensor system closely agree with those obtained using the tachometer. Since Fig. 13(b) and (c) that compute the x and y coordinates of the axis of rotation is sensitive to the difference of the two sensor readings, the computed data of the x and y coordinates are somewhat noisy. These noises were filtered using a digital filter. As compared in Figs. 11(b) and 12(b), the filtered x and y coordinates of the shaft axis are identical regardless of the input wave forms. The computational cycle time including data saving and display is in the order of 4 ms.

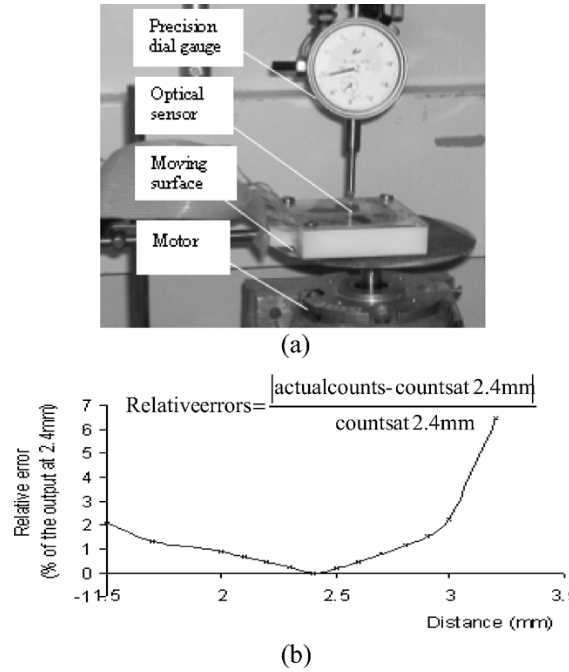

Fig. 9. Effects of sensor-surface spacing. (a) Test setup. (b) Test results.

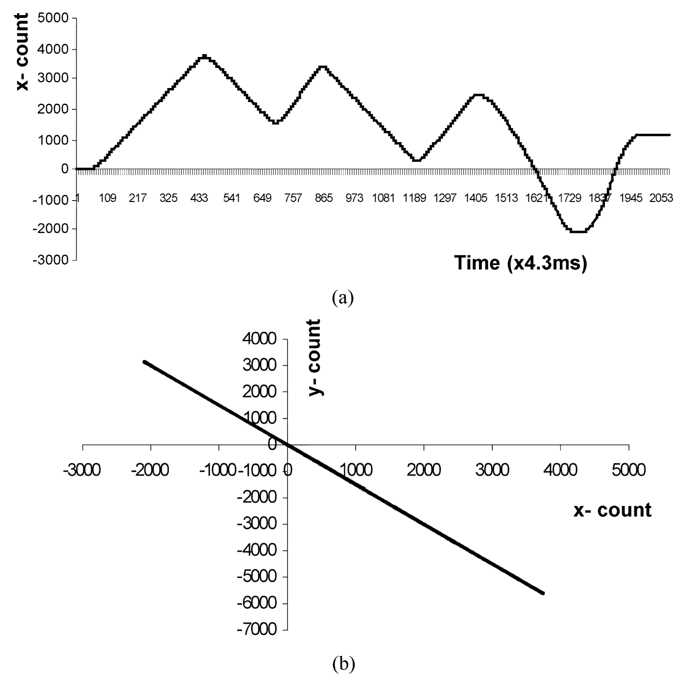

Fig. 10. Test results of repeatability. (a) x-counts for an arbitrary trajectory. (b) Local (x- and y-counts) as viewed by the sensor.

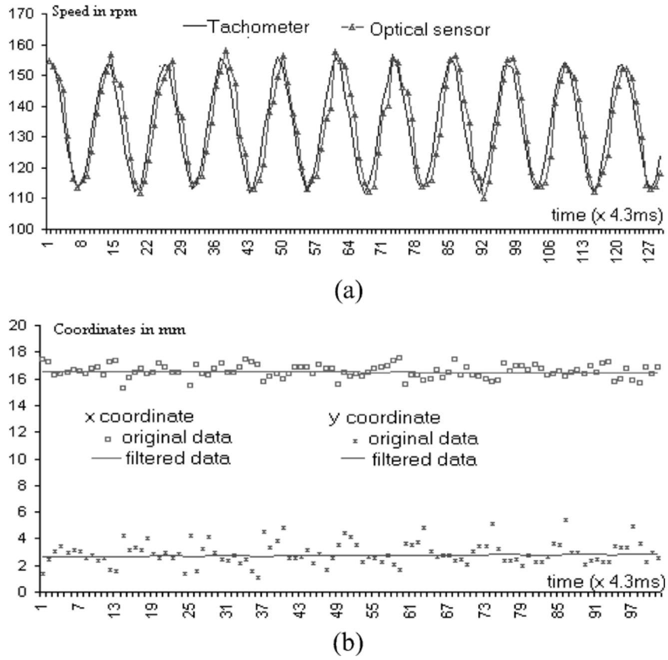

Fig. 11. 3-DOF sensor response to sinusoidal input. (a) Angular speed in rpm. (b) x and y coordinates in mm.

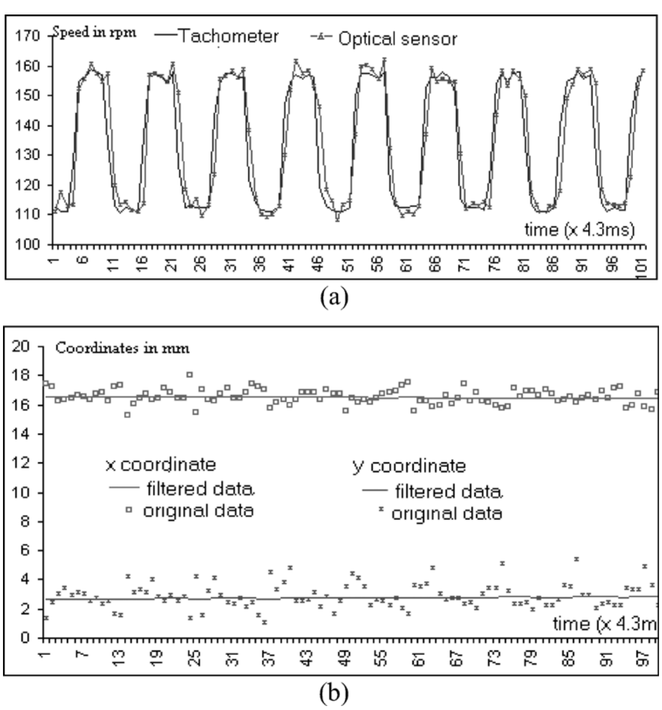

Fig. 12. 3-DOF Sensor response to sinusoidal input. (a) Angular speed in rpm. (b) x and y coordinates in mm.

E. Measuring Three-DOF Spherical Orientations

Experiments for testing the spherical sensor were carried out on the wrist apparatus [11] shown in Fig. 13, which uses three stepper motors to provide 3-DOF rotations. These motors (referred as X, Y, and z motors) drive the spherical shell via a universal joint. With half-stepping and a 9:1 timing-belt pulley reduction, the X and Y motions have a resolution of 0.1° per step. The z-motor driven via a microstepping controller rotates

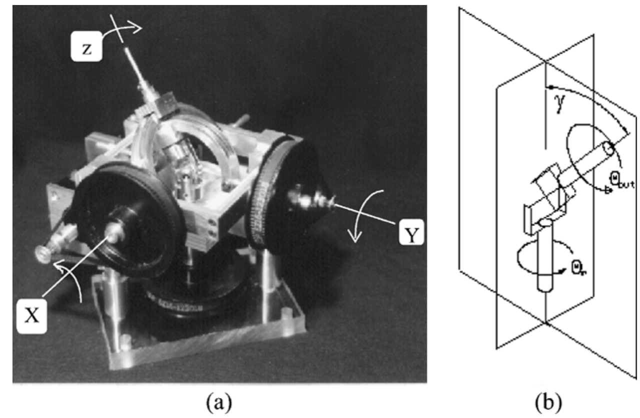

Fig. 13. Three-DOF wrist actuators. (a) Wrist structure; (b) universal joint.

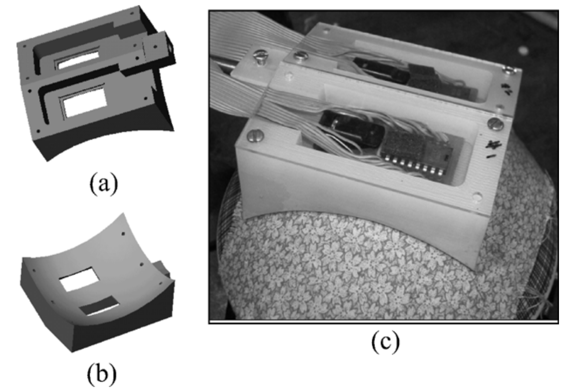

Fig. 14. CAD model and prototype mechanical holder. (a) Top. (b) Bottom. (c) Experimental prototype.

TABLE II
PARAMETERS OF EXPERIMENTAL PROTOTYPE

Design parameters	Values
Radius of spherical shell, R, mm (inch)	75 (3)
Sensor-surface spacing, mm	2
Sensor Resolution , counts per mm (counts per inch)	19.49 (495)
Sensor frame-rate, fps	1,500
Computer cycle time, ms	4.3538
Spacing between sensors, θ_y, degrees	22
Maximum γ in degrees	45

at a resolution of 10 000 steps per inch (0.036°) with respect to the X and Y motors. The shaft that rotates the shell covers a cone of 70° motors. To match the moving surface, the two sensors are housed in a holder fabricated using stereography as shown in Fig. 14, where the shell is covered with a piece of fabrics to provide a random-featured surface. Other values of the design parameters are summarized in Table II.

The following features were used to align the sensors with the shell.

1) The sensors face down with their optical axes pointing toward and intersecting at the center of the spherical shell.
2) The X_s-axes of both sensors are parallel to the X-axis such that both sensors have the same readouts in responding to rotations about the Y-axis only.
3) Since a single optical sensor is indifferent to rotations about its own optical axis, sensor #1 provides no information when the rotor shaft (or the z-axis) is in line with the Z-axis.

TABLE III
SUMMARY OF EXPERIMENTAL RESULTS

Rotations	(ϕ_X, ϕ_Y, ϕ_z) in degrees		
	Specified	**Measured**	**Max. error**
ϕ_X	(0, 0, 0)	(0.00, 0.00, 0.00)	
	(10, 0, 0)	(10.30, -0.09, 0.54)	0.54
	(-10, 0, 0)	(-10.26, -0.10, 0.04)	0.26
	(10, 0, 0)	(10.23, -0.19, 0.95)	0.95
	(-10, 0, 0)	(-10.30, 0.12, 0.10)	0.30
	(0, 0, 0)	(0.01, -0.10, 0.31)	0.31
ϕ_Y	(0, 0, 0)	(0, 0, 0)	
	(0, 10, 0)	(0.22, 10.04, -0.32)	0.32
	(0, -10, 0)	(0.02, -10.10, -0.17)	0.10
	(0, 10, 0)	(0.07, 10.20, 0.35)	0.35
	(0, -10, 0)	(0.32, -10.09, 0.32)	0.32
	(0, 0, 0)	(0.12, -0.14, 0.21)	0.21
ϕ_X, ϕ_Y	(0, 0, 0)	(0, 0, 0)	
	(10, 10, 0)	(10.10, 10.29, 0.20)	0.29
	(-10, -10, 0)	(-10.03, -10.04, -0.08)	0.08
	(10, 10, 0)	(10.03, 10.01, 0.13)	0.13
	(-10, -10, 0)	(-10.02, -10.01, 0.20)	0.20
ϕ_z	(0, 0, 0)	(0, 0, 0)	
	(0, 0, -10)	(0.01, 0.00, -10.07)	0.07
	(0, 0, -20)	(0.03, 0.00, -19.85)	0.15
	(0, 0, -30)	(0.10, 0.03, -29.83)	0.17
	(0, 0, -40)	(0.18, 0.10, -40.01)	0.18
	(0, 0, -50)	(0.30, 0.38, -50.00)	0.38
ϕ_X, ϕ_z	(0, 0, 0)	(0, 0, 0)	
	(0, 10, -10)	(0.15, 10.43, -9.86)	0.43
	(0, -10, -20)	(0.30, -10.34, -20.78)	0.78
	(0, 10, -30)	(0.51, 10.08, -30.00)	0.51
	(0, -10, -40)	(0.87, -10.21, -41.12)	1.12
ϕ_X, ϕ_Y, ϕ_z	(0, 0, 0)	(0, 0, 0)	
	(10, 10, -10)	(10.56, 11.60, -9.70)	1.60
	(-10, -10, -20)	(-8.97, -8.58, -21.09)	1.42
	(10, 10, -30)	(11.60, 11.60, -29.2)	1.60

Six different types of rotations (about the individual X, Y, and z axes, the combination of X- and Y-axes, X- and z-axes, and X-, Y-, and z-axes) were experimentally tested. Two types of motion commands are used; the first involves a step change of ϕ_X or ϕ_Y for α and γ going through 0 from $10°$ to $-10°$. The second is a monotonic decrement of ϕ_z. For each test, the initial location of the shaft is at $\alpha = \gamma = 0$. The rotation angles (ϕ_X, ϕ_Y, ϕ_z) of the X, Y, and z motors, along with the rotor shaft location (γ, α), are calculated and used as commands to drive the three steppers. Equations (20) and (22) are then used to recover the rotations (ϕ_X, ϕ_Y, ϕ_z) from the sensors. The results comparing the specified values and the computed data for the six types of rotations are summarized in Table III. Graphical time representations of the experimental results are shown in Fig. 15, which correspond to the last case in Table III. Fig. 15(a) shows the four sensor readouts in counts. Fig. 15(b) displays the computed rotations about X, Y, and z axes. The shaft position (X_p, Y_p, Z_p) and inclination (γ, α) are given in Fig. 15(c) and (d), respectively.

As shown in Table III, the maximum errors are less than $1°$ (in the order of the stepper resolution) for the four cases (X, Y, XY, z) that require only one sensor. The last two cases (X–z, Xyz) that require two sensors exhibit a larger error (but within $1.6°$) as the two optical axes might have not met at the center of the moving surface as assumed.

Fig. 15(d) shows that the computed shaft inclination is sensitive around $\gamma = \alpha = 0$. Simulation was carried out using the

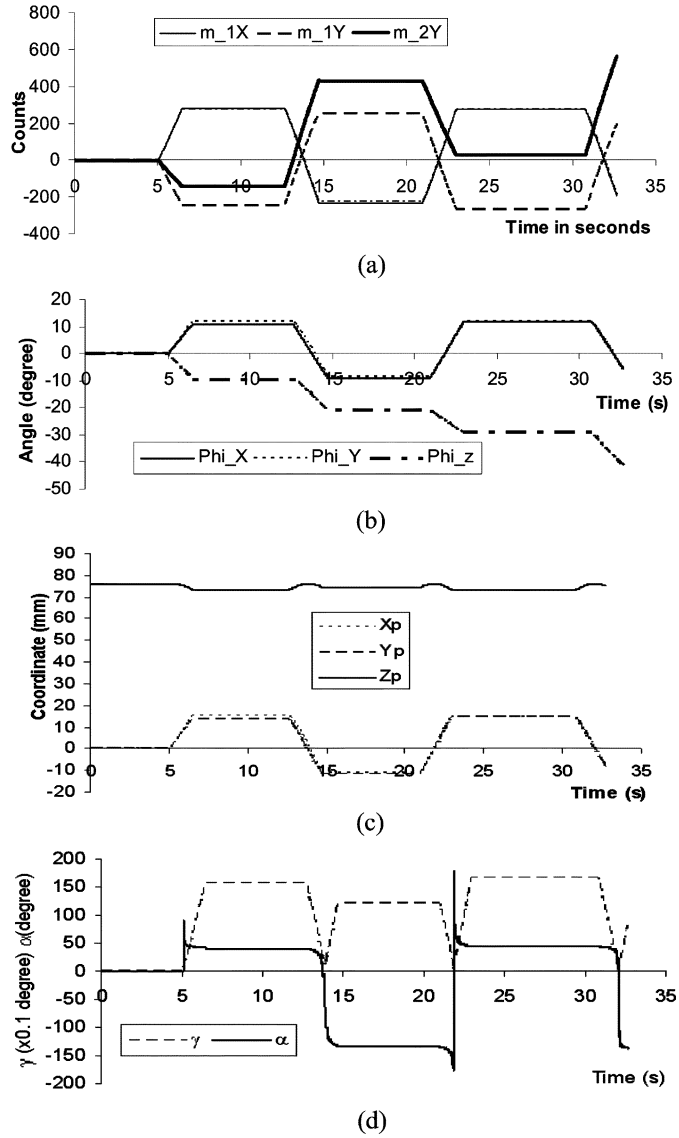

Fig. 15. Experimental results. (a) Sensor counts; (b) rotations about X, Y and z axes; ϕ_X, ϕ_Y, ϕ_z; (c) X_p, Y_p and Z_p as a function of time; (d) α and 10γ as a function of time.

inverse kinematics, equations (20)–(22), to study the effects of missed counts on the computation. In each simulated calculations, white noises $(-4, 0)$ in counts were superimposed to each of the four sensor readouts (all of which were assigned equal values, corresponding to a shaft inclination of $45°$). The sensor data (with and without noises) were then used to compute the angles (ϕ_X, ϕ_Y, ϕ_z), the inclination (α, γ), and the shaft position $\mathbf{r}_P(x_p, y_p, z_p)$. Fig. 16(a)–(c) summarizes the computed differences between with and without noises. As shown in Fig. 16(a), missed counts have a larger influence in ϕ_z than in ϕ_X or ϕ_Y; in Fig. 16(b), the computation of α is very sensitive in the neighborhood of $\gamma = 0$ at which any missed count could cause $\alpha = \pi/4$ to $\alpha = \pi - (\pi/4) = 3\pi/4$ and vice versa, which well agrees with the experimental results in Fig. 15(d). As shown in Fig. 16(c), it is preferable to use the shaft position; the influence of missed counts has been kept within 200 μm (4 times the resolution of the optical sensor or approximately 50 μm per count).

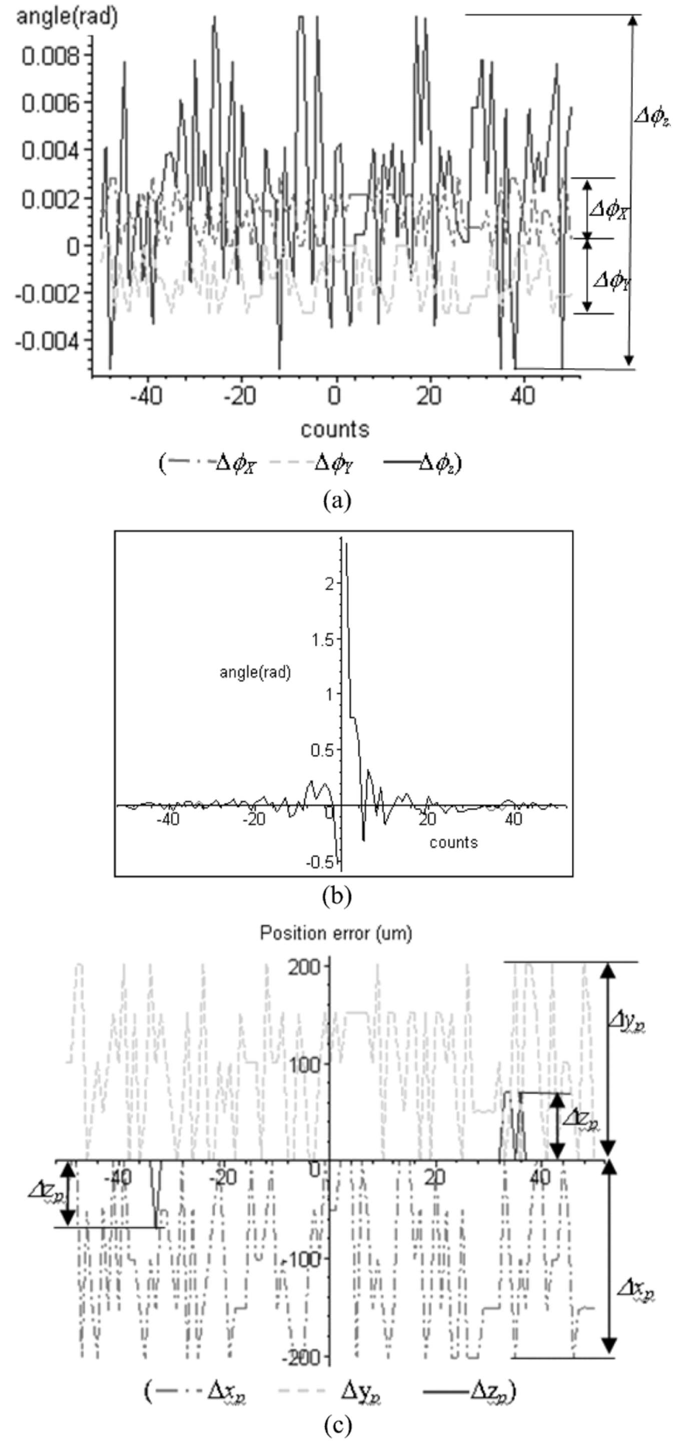

Fig. 16. Simulation results. (a) Errors in ϕ_X, ϕ_Y, ϕ_z. (b) Errors in α and γ. (c) Errors in x_p, y_p, z_p.

V. Conclusion

The design concept and analysis of a dual-sensor system capable of measuring three-DOF planar motions in real time has been presented. The dual-sensor system, which detects microscopic changes in consecutive images, computes the angular displacement of a moving surface and the instantaneous center of rotational axis. An experimental prototype has been developed and tested. The concept feasibility of the dual-sensor system for measuring 3-DOF planar motions has been demonstrated experimentally. A detailed experimental analysis has been presented, which not only helps to provide a better understanding of the sensor but also identifies key design parameters that significantly influence its resolution and repeatability. It is expected that the prototype dual-sensor system has an immediate application in measuring the 3-DOF orientations of a spherical motor.

References

[1] *Quadrature Decoder/Counter Interface ICs, Technical Data*, Agilent Technologies, Inc., 1999.
[2] *Solid-State Optical Mouse Sensor With PS/2 and Quadrature Outputs, Technical Data*, Agilent Technologies, Inc., 2001.
[3] M. Bidlville, E. Raeber, J. Arreguit, H. Buczek, F. Van Shaik, F. Bauduin, and D. O'Keeffe, "Pointing device utilizing a photo-detector array," U.S. Patent 5,703,356, Dec. 30, 1997.
[4] Copley Motion Controller (DC Brush Servo Amplifier, Model 412) [Online]. Available: http://www.copleycontrols.com/motion/amplifiers
[5] X. Fernandez, J. Amat, and J. M. Fuertes, "Research on small fiducial mark use for robotic manipulation and alignment of ophthalmic lenses," in *Proc. IEEE Int. Conf. Emerging Technologies and Factory Automation*, Barcelona, Spain, 1999, pp. 1143–1146.
[6] *DAS-1600/1400 Series User's Guide*, Keithley.
[7] *KPCI-3130 PCI Analog Output Board User's Manual*, Keithley.
[8] K.-M. Lee, "Orientation sensing system and method for a spherical body," U.S. Patent 5 319 577, Apr. 25, 1995.
[9] K.-M. Lee and R. Blenis, "Design concept and prototype development of a flexible integrated vision system," *J. Robotic Syst.*, vol. 11, no. 5, pp. 387–398, 1994.
[10] J. McCarthy, "Space vision system," in *Proc. 29th Int. Symp. Robotics: Advanced Robotics: Beyond 2000*, Birmingham, U.K., Apr./May 1998, pp. 323–325.
[11] M. Klement, "Development of a three DOF vision-based absolute orientation sensor," M. S. thesis, Georgia Tech., Atlanta, GA, 1997.

Kok-Meng Lee received the B.S. degree in mechanical engineering from the State University of New York at Buffalo in 1980 and the M.S. and Ph.D. degrees in mechanical engineering from the Massachusetts Institute of Technology, Cambridge, in 1982 and 1985, respectively.

He has been with the Georgia Institute of Technology, Atlanta, since 1985. As a Professor of mechanical engineering, his research interests include system dynamics and control, robotics, automation and opto-mechatronics. He holds seven U.S. patents.

Dr. Lee served as an Associate Editor of the *IEEE Robotics and Automation Society Magazine* from 1994 to 1996, Associate Editor of the IEEE Transactions on Robotics and Automation from 1994 to 1998, and as a Technical Editor of the IEEE/ASME Transactions on Mechatronics from 1995 to 1999. He has held representative positions within the IEEE Robotics and Automation Society. He founded and chaired the Technical Committees on Manufacturing Automation (1996 to 1998) and on Prototyping for Robotics and Automation. He served as Chair or Co-Chair for numerous international conferences. He has received a Presidential Young Investigator (PYI) Award, Sigma Xi Junior Faculty Award, International Hall Of Fame New Technology Award, and the Woodruff Faculty Fellow. He was also recognized as an advisor for six Best Student Paper Awards and a Best Thesis Award.

Debao Zhou received the B.Eng. and M.Eng. degrees in mechanical engineering from Tsinghua University, Beijing, China, in 1993 and 1996, respectively, the M.S. degree in mechanical engineering from the Georgia Institute of Technology, Atlanta, in 2003, and the Ph.D. degree in mechanical and production engineering from Nanyang Technological University, Singapore, in 2004.

His research interests include robotics, noncontact sensing, intelligent control, and system dynamics.